



Detecting seismogenic stress evolution and constraining fault zone rheology in the San Andreas Fault following the 2004 Parkfield earthquake

Taka'aki Taira,¹ Paul G. Silver,¹ Fenglin Niu,² and Robert M. Nadeau³

Received 3 May 2007; revised 22 September 2007; accepted 14 December 2007; published 8 March 2008.

[1] We investigate temporal changes in seismic scatterer properties at seismogenic depth attributed to the 2004 M 6 Parkfield earthquake, making use of the San Andreas Fault Observatory at Depth repeating-earthquake target sequences, as well as nearby similar-earthquake aftershock clusters. We use a two-step process: (1) observing temporal variations in the decorrelation index, $D(t)$, reflecting changes in the scattered wavefield of repeating-earthquake sequences and (2) estimating the spatial distribution of time-dependent scatterers by using a larger-aperture source array. We focus on three scatterers exhibiting clear time dependence, using pairs of earthquakes that span or follow the 2004 Parkfield earthquake. They are found to be located on the fault at the northernmost extent of coseismic rupture, beneath Middle Mountain, with a depth range of 11 to 17 km. The shallowest and most prominent scatterer is located near a region of increased Coulomb stress, as well as significant postseismic slip following the 2004 Parkfield earthquake, and a large $M = 5$ aftershock. The other two deeper ones are also in regions of increased Coulomb stress. We show that $D(t)^{1/2}$ is expected to be proportional to the level of stress in the fault zone, and then we constrain the form of fault zone rheology by comparing the time dependence of $D(t)^{1/2}$ with geodetic or seismic measures of strain rate, assuming a power law rheology between stress and strain rate characterized by exponent n . Such a comparison yields n ranging from 1.6 through 3.3, a value that is more consistent with ductile behavior, rather than frictional sliding, at the base of the seismogenic zone.

Citation: Taira, T., P. G. Silver, F. Niu, and R. M. Nadeau (2008), Detecting seismogenic stress evolution and constraining fault zone rheology in the San Andreas Fault following the 2004 Parkfield earthquake, *J. Geophys. Res.*, *113*, B03303, doi:10.1029/2007JB005151.

1. Introduction

[2] Observing transient stress changes at seismogenic depth is a key aspect to understanding the nucleation process of earthquakes. One approach to making such observations is to detect temporal changes in the medium that reflect the stress-induced opening or closing of fractures. Scattered waves effectively sample fractures as seismic scatterers when their wavelengths are comparable to fracture size. An analysis of temporal variations in the scattered wavefield, in principle, has the capability of providing the time evolution of the stress field due to changes in crack properties.

[3] To detect a reliable temporal change in the medium, repeating earthquakes and repeated artificial sources have been recently used to minimize the errors due to changes in source location and mechanism. Using temporal changes in traveltimes, a number of studies have revealed earthquake-

related coseismic damage of rock and subsequent healing nearby fault zones [e.g., *Li et al.*, 1998; *Vidale and Li*, 2003]. Temporal variations of traveltimes from strong motion-induced shallow cracking have been also reported [e.g., *Rubinstein and Beroza*, 2004, 2005; *Peng and Ben-Zion*, 2006]. *Rubinstein and Beroza* [2004] showed a correlation between temporal variation in traveltime and intensity of strong motion following the 1989 M 7.1 Loma Prieta earthquake, suggesting that this temporal variation attributed to this mechanism.

[4] On the other hand, stress-induced temporal changes in traveltimes have been observed [e.g., *Dodge and Beroza*, 1997; *Baisch and Bokelmann*, 2001; *Yamamura et al.*, 2003; *Silver et al.*, 2007]. *Niu et al.* [2003] detected systematic temporal variations in the scattered wavefield, and hypothesized that this represented stress-induced migration of fluid caused by the 1993 Parkfield aseismic transient. Laboratory studies have also demonstrated the ability to detect transient stress seismically [e.g., *Freund*, 1992; *Sarkar et al.*, 2003; *Grêt et al.*, 2006]. In principle, detecting stress-induced changes in scatterers is not only important in its own right, but, combined with measures of strain rate, from geodesy or other means, it is possible to constrain the form of fault zone rheology.

¹Department of Terrestrial Magnetism, Carnegie Institution of Washington, Washington, D. C., USA.

²Department of Earth Science, Rice University, Houston, Texas, USA.

³Berkeley Seismological Laboratory, University of California, Berkeley, California, USA.

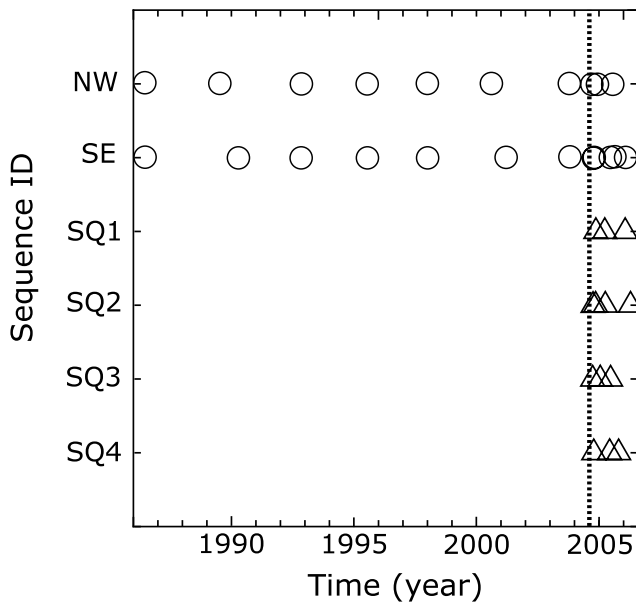


Figure 1. Event occurrence times. NW and SE sequences denote the SAFOD repeating earthquakes (circles), while SQ1, SQ2, SQ3, and SQ4 are repeated-aftershock sequences (triangles). The dashed line is the occurrence time of the 2004 Parkfield earthquake.

[5] An ideal test for detecting stress-induced changes in seismic scatterers and constraining fault zone rheology properties has been provided by the 28 September 2004 M 6.0 Parkfield earthquake, California for four reasons. First, the coseismic and postseismic slip models have been well determined [Johanson *et al.*, 2006, Liu *et al.*, 2006], so that we can retrieve a reliable stress perturbation model of the 2004 Parkfield earthquake. Second, many repeating-earthquake sequences have been detected in the Parkfield region [Nadeau and McEvilly, 1999, 2004]. Third, the 2004 Parkfield earthquake produced numerous aftershock sequences with similar source mechanisms [Li *et al.*, 2006]. Finally, continuous geodetic data by a dense network of GPS receivers are available [Langbein *et al.*, 2006].

[6] In this study, we first detect temporal variations in the scattered wavefield of local earthquakes, using repeating-earthquake sequences (event spacing less than 5 m), and next locate the corresponding time-varying scatterers using a larger-aperture source array (horizontal aperture size ~ 100 m \times 20 m), which we then compare to the slip distributions for the coseismic and postseismic components of the 2004 Parkfield earthquake. We finally address the time evolution of the stress field at seismogenic depth following the 2004 Parkfield earthquake, showing that it is most consistent with a ductile fault zone rheology.

2. Data and Analysis

2.1. Data Set

[7] To detect time-dependent scatterers, we have made use of the two repeating-earthquake sequences known as the “target sequences” studied by the San Andreas Fault Observatory at Depth (SAFOD), termed the northwestern (NW) and southeastern (SE) sequences [Nadeau *et al.*,

2004]. During the study period, the NW and SE sequences contained 10 and 12 repeating earthquakes, respectively (Figure 1). The average magnitude of these repeating earthquakes is approximately 2.0 (Table 1), corresponding to a rupture patch radius of about 50 m for a 3 MPa stress drop, assuming a circular crack model [Eshelby, 1957]. These two sequences are separated from each other by around 50 m in horizontal distance along the strike of the San Andreas Fault. The depth of these sequences is approximately 1.5 km.

[8] There are over 60 aftershocks whose waveforms and locations are similar to those in the SAFOD target sequences, and several groups of these similar events are also sequences of repeating earthquakes. We used the seismic data from the NW and SE repeating earthquakes to examine temporal properties of the scattered wavefield, and then utilized these data, along with those from the additional repeated-aftershock sequences, to estimate the spatial properties of time-dependent scatterers. We analyzed seismograms recorded by the borehole seismometers of the High-Resolution Seismic Network (HRSN) [Karageorgi *et al.*, 1992] (Figure 2) because they reduce the influence of superficial coseismic damage, compared to surface instruments [Rubinstein and Beroza, 2005].

2.2. Detecting Temporal Change in Scattered Wavefield

[9] Using repeating earthquakes with short recurrence interval, we are able to examine the characteristics of temporal changes in the scattered wavefield with high resolution, for example, three and five events have been detected as repeating earthquakes in the NW and SE sequences during post the 2004 Parkfield earthquake to 2007 (Figure 1). Since the HRSN has been operated since 1987, the seismic records for the first repeating earthquakes (occurring in 1986) in the NW and SE sequences are not available. Note that we did not have several seismic records from 1998 through 2001 because the HRSN recording system was not operating during this period [Nadeau *et al.*, 2004]. We also did not utilize a few seismic records from events occurring between 2001 and 2003 because the high-sampling data (250 Hz) were not available.

[10] We first identified temporal variations in the scattered wavefield by measuring the dissimilarity in waveform pairs from the NW and SE sequences. We used a sliding-window waveform cross-correlation analysis with a 0.5-s time window, from which we obtained a lag time, $\tau(t)$, and decorrelation index, $D(t)$, where t is elapsed time on the seismogram; $\tau(t)$ corresponds to the lag for which the cross-correlation function reaches its maximum value, $C_{\max}(t)$, and $D(t) = 1 - C_{\max}(t)$ [Niu *et al.*, 2003]. Each waveform was aligned by its direct P arrival and was interpolated to 10,000 samples per second. A 20% cosine taper was applied to each time window.

[11] The parameter $\tau(t)$ can be interpreted as the mean traveltime perturbation of the lag times, τ_i , associated with the individual scattered phases in the time window, while $D(t)$ can be defined as $\omega^2 s_\tau^2 / 2$ where s_τ and ω are the standard deviation of τ_i and the characteristic frequency of the scattered phases, respectively [Snieder *et al.*, 2002]. Thus $\tau(t)$ and $D(t)^{1/2}$ are proportional to the mean and standard deviation of a weighted distribution of lag times, respectively. A constant velocity reduction in the back-

Table 1. Average Hypocenters and Magnitudes for Sequences Used in this Study

Sequence	Latitude, ^a deg	Longitude, ^a deg	Depth, ^{a,b} km	Magnitude
NW	35.9810	-120.5468	1.472	2.1
SE	35.9807	-120.5464	1.476	2.0
SQ1	35.9811	-120.5470	1.502	1.0
SQ2	35.9811	-120.5470	1.493	1.4
SQ3	35.9806	-120.5462	1.483	1.2
SQ4	35.9809	-120.5466	1.469	1.1

^aAverage hypocenter of each sequence was evaluated by using earthquakes after October 2001.

^bDepth is below mean sea level.

ground medium should yield a linear trend in $\tau(t)$ and $D(t) = 0$, given a short time window for calculating $\tau(t)$ and $D(t)$.

[12] On the other hand, *Niu et al.* [2003] showed through numerical experiments that isolated spikes in $\tau(t)$ and $D(t)$ can be explained by local changes in the location of a scatterer or by a velocity reduction around the scatterer. Our interest is in detecting discrete scatterers that permit the imaging of the fault zone properties at seismogenic depth, rather than changes in the background medium. We have therefore focused on detection of isolated spikes in $D(t)$ and, to a lesser extent, $\tau(t)$.

[13] To estimate $D(t)$ and $\tau(t)$, we made use of the final event in each sequence as a reference. We examined temporal changes in average $D(t)$ of the S coda with a 4.0-s time window from around 1.0 s after the direct S arrival for all available HRSN borehole stations. We found that the average $D(t)$ for 11 of 13 stations show a systematic decrease following the 2004 Parkfield earthquake (Figure 3). Since the average $D(t)$ for stations VCA and RMN are highest and show clear systematic temporal decays following the 2004 Parkfield earthquake, the seismic data recorded at stations VCA and RMN were used for further analysis. As shown in Figure 3, the average $D(t)$ for half of the HRSN stations systematically increases in middle 2005. We speculate that they are response to another temporal change on the San Andreas Fault, and this is being addressed in a subsequent manuscript.

[14] For station VCA, we detected several isolated spikes in $D(t)$ (Figure 4b), and found a subset of time-varying scattered phases for pairs of repeating earthquakes spanning or following the 2004 Parkfield earthquake. Since the waveforms in the NW sequence are similar to those in the SE sequence, we can clearly identify the same isolated spike in $D(t)$ for the two sequences. Plots of $\tau(t)$ also show corresponding spikes and they additionally exhibit an increasing linear trend with increasing elapsed time (Figure 4c).

[15] Such a linear trend in $\tau(t)$ has already observed following the 2004 Parkfield earthquake [*Rubinstein and Beroza*, 2005; *Li et al.*, 2006] and can be related to a reduction in shear wave velocity due to the opening of cracks in superficial layers by strong ground shaking [*Rubinstein and Beroza*, 2005] or damaged rocks by the coseismic slip [*Li et al.*, 2006]. The negative linear trends are seen on lag times for the 1990 and 1995 events (Figure 4c), which implies that the velocity reduction did not recover fully by 2006.

[16] We assumed that the effect of a near-surface layer beneath the station is to generate a constant velocity perturbation to each of the phases arriving at the station. As noted above, this should produce a linear trend in $\tau(t)$ with elapsed time but no effect on $D(t)$, while isolated spikes in $D(t)$ (or $\tau(t)$) can be the response to local changes in the medium. For this reason we assume that $\tau(t)$ always contains the contribution of this surface layer, which we seek to avoid.

[17] Isolated spikes in $D(t)$ are not seen before the 2004 Parkfield earthquake except for a few subtle features in the S coda (Figure 4b). Large values of $D(t)$ near direct P and S arrivals were caused by clipped signals on the raw seismograms for earthquakes occurring before 1998 due to limited instrumental dynamic range.

[18] We aligned the P waves by the onset times of the raw traces, so that this distortion does not affect the alignment. We then corrected for instrument response and converted the records to displacement seismograms. Although this procedure causes distortions in waveforms near the clipped

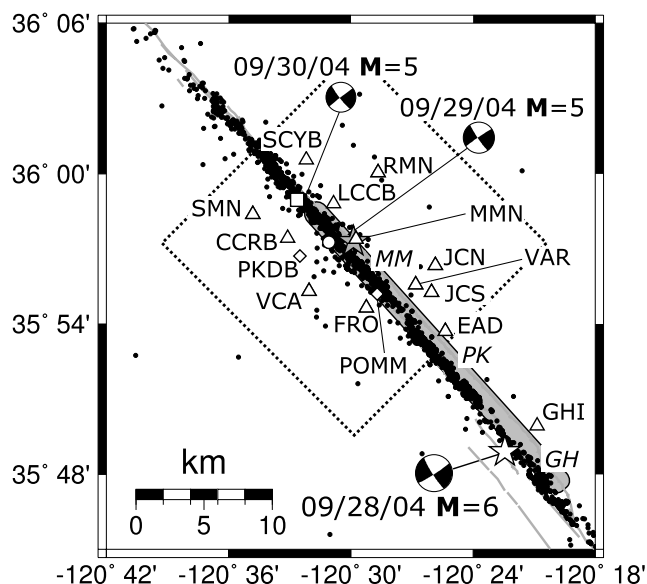


Figure 2. Map view of the source region including the SAFOD repeating earthquakes as well as repeated aftershocks (square) used in this study and borehole seismic stations (triangles). Open and gray stars are the epicenters of the 2004 and 1966 Parkfield earthquakes. The dashed square is the model space for estimating locations of scatterers. Diamonds denote GPS stations, and open circle is the location of the repeating-earthquake sequence for estimating slip rate at depth. Dots are epicenters of aftershocks of the 2004 Parkfield earthquake [*Thurber et al.*, 2006], and gray line is the surface trace of the San Andreas Fault (U.S. Geological Survey and California Geological Survey, Quaternary fault and fold database for the United States, 2006, <http://earthquakes.usgs.gov/regional/qfaults/>). Gray area is the surface rupture zone of the 2004 Parkfield earthquake. Also shown are the focal mechanisms for the 2004 Parkfield earthquake and two $M = 5$ aftershocks [*Langbein et al.*, 2005]. Place names are abbreviated MM, Middle Mountain; PK, Parkfield; and GH, Gold Hill.

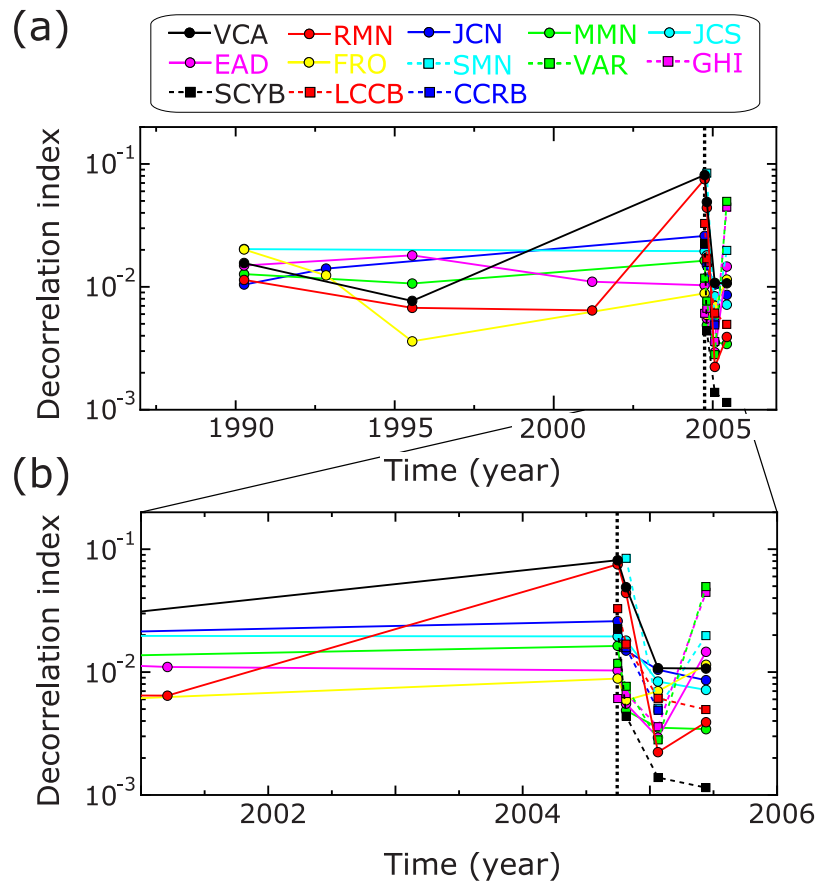


Figure 3. Temporal change in average $D(t)$ of S coda with a 4.0-s time window (a) from 1987 through 2007 and (b) from 2001 through 2006. The dashed line is the occurrence time of the 2004 Parkfield earthquake.

signals, we confirmed that there is no influence on the S coda, which is far from the distorted arrivals.

[19] The waveforms recorded at station RMN also show similar temporal changes in wavefields following the 2004 Parkfield earthquake (Figure 5a). The decorrelation indexes and lag times increased after the 2004 Parkfield earthquake and subsequently decayed (Figures 5b and 5c). While we assume that the variation begins with the 2004 Parkfield earthquake, we were able to place an observational constraint on the onset by using an event which occurred in 2001. The decorrelation index for the pair of events in 2001 and 2006 is nearly zero from the direct P wave to late S coda (Figure 5b), which strongly suggests that the observed temporal changes are most likely due to the 2004 Parkfield earthquake. For seismic records at station RMN, we identified the same time-varying scattered phases observed at station VCA, by using the predicted traveltimes from the corresponding time-dependent scatterers (see section 2.3).

[20] We additionally chose four sequences (SQ1 to SQ4) of repeated aftershocks. The average magnitudes of SQ1, SQ2, SQ3, and SQ4 are 1.0, 1.4, 1.2, and 1.1, respectively (Table 1). These sequences contain 3 or 4 earthquakes (Figure 1) and they occurred nearby the NW and SE sequences. The same temporal changes were found from all of the repeated-aftershock sequences. The observation of temporal variation for different sequences strongly suggests that the detected time-varying scattered phases represent the

response to changes in crustal structure rather than in earthquake location or source mechanism.

[21] To further rule out hypocenter variability as a potential cause of temporal change, we also measured the average (over stations) of $D(t)$, $\langle D(t) \rangle$, of the clearly observed direct S waves for each repeating earthquake with respect to the final event in the SAFOD sequence, by using seismic records at available HRSN stations. We found that $\langle D(t) \rangle$ are 1–2 orders of magnitude less than $D(t)$ for the identified time-dependent scattered phases for events occurring 2 d after the 2004 Parkfield earthquake. This result shows high source similarity among the repeating earthquakes in the SAFOD target sequences, suggesting that the hypocenter variability in our data set should be small enough for examining temporal changes in the medium. To calculate $\langle D(t) \rangle$, we excluded seismic records having the clipped signals near the direct S waves.

[22] For the prominent time-varying scattered phases (hereafter called X1, X2, and X3), we found that the temporal variation appears to be restricted to the time interval from the occurrence of the 2004 Parkfield earthquake to 4 months after. The waveforms of these scattered phases for later earthquakes are nearly identical to those for earthquakes occurring before the 2004 Parkfield earthquake. In other words, the scattered wavefields have changed following the 2004 Parkfield earthquake, and then returned

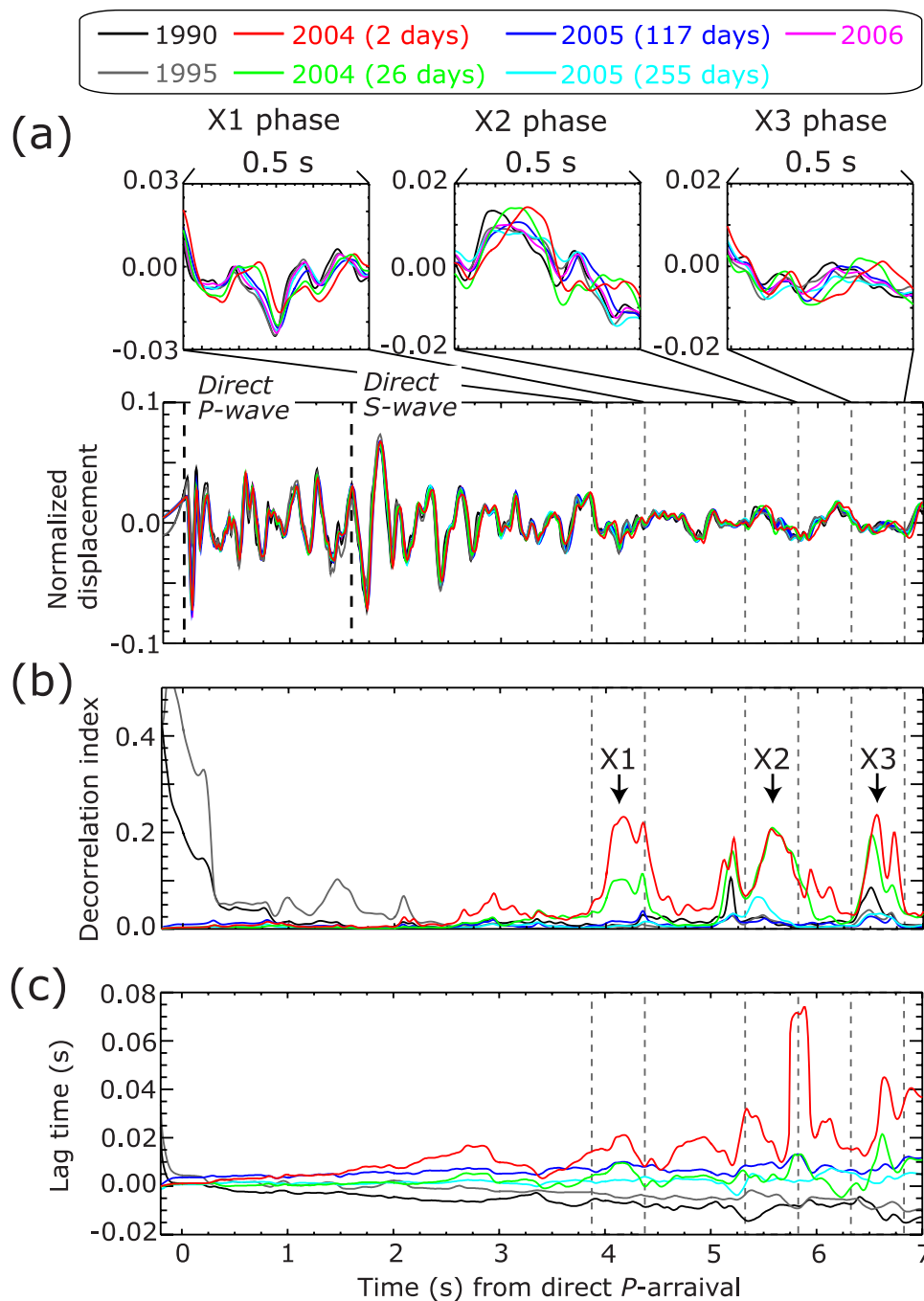


Figure 4. (a) Observed vertical component seismograms recorded at station VCA for the SE target sequence, (b) their decorrelation indexes, $D(t)$, and (c) lag times, $\tau(t)$, by using a sliding time window of 0.5 s. Waveform colors indicate earthquake occurrence dates: black, 7 April 1990; gray, 19 July 1995; red, 30 September 2004; green, 24 October 2004; blue, 23 January 2005; right blue, 10 July 2005; and purple, 28 January 2006. The event occurring on 28 January 2006 was used as a reference to measure $D(t)$ and $\tau(t)$. Also shown in parentheses are elapsed days after the 2004 Parkfield earthquake.

to the original state 4 months after the 2004 Parkfield earthquake.

[23] For these three X1, X2, and X3 phases, the temporal changes in wavefield are strongest on the vertical component (Figure 6), which implies the wave type of time-varying scattered phases between scatterers to stations is a P wave. At the same time, the arrivals of these phases are

found in the S coda where S - P scattering is more prevalent than P - P one [e.g., Sato and Fehler, 1998]. We therefore assumed the scattering modes of X1, X2, and X3 phases to be S - P .

[24] We seek to characterize the time dependence of this decay process, making use of $D(t)$. We expect $D(t)$ to be a proxy for seismogenic stress, $\sigma(t)$. As has been noted

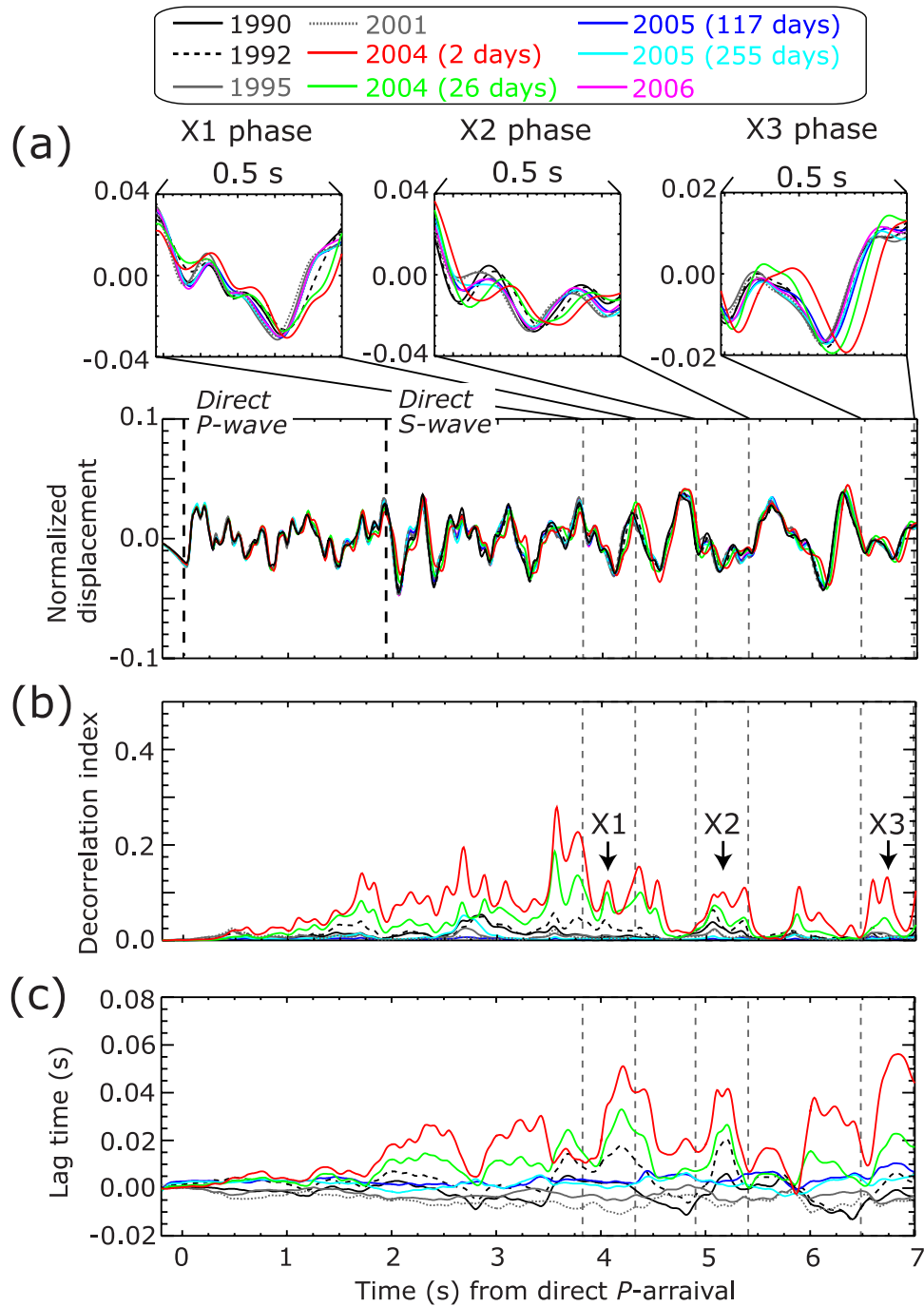


Figure 5. Same as Figure 4 except for station RMN and two additional waveforms: (1) 3 November 1992 (black dashed line) and (2) 17 March 2001 (gray dotted line).

previously [Snieder et al., 2002], for characteristic frequency, ω , $D(t) = \omega^2 s_r^2 / 2$, where s_r is the standard deviation of lag times among scattered phases in a time window. For small changes in the medium, the fractional perturbation in seismic velocity, $\delta\nu/V$ is approximately equal to the negative of the fractional change of traveltime, τ/T , i.e., $\delta\nu/V \sim -(\tau/T)$ given constant velocity reduction, where T is a traveltime for a specific phase and τ is its lag time between two seismograms.

[25] In the case of a nonconstant velocity change, we assume that the mean lag time $\tau(t) = \langle \tau_i \rangle$ in the time

window can be treated as a mean perturbation in velocity, $\langle \delta\nu \rangle$. We focused on the observed isolated spikes in $D(t)$ and $\tau(t)$ which can be interpreted as local changes in the medium rather than variations in the entire medium. Because $\tau(t)$ also has potential contributions due to near-receiver structure, as noted above, we used isolated spikes in $D(t)$ for further analysis.

[26] We assumed that lag times have a probability density function, $P(\tau_i)$, right after the 2004 Parkfield earthquake, due to a perturbation in the medium. We expect the overall magnitude of the perturbation to decay to zero over time,

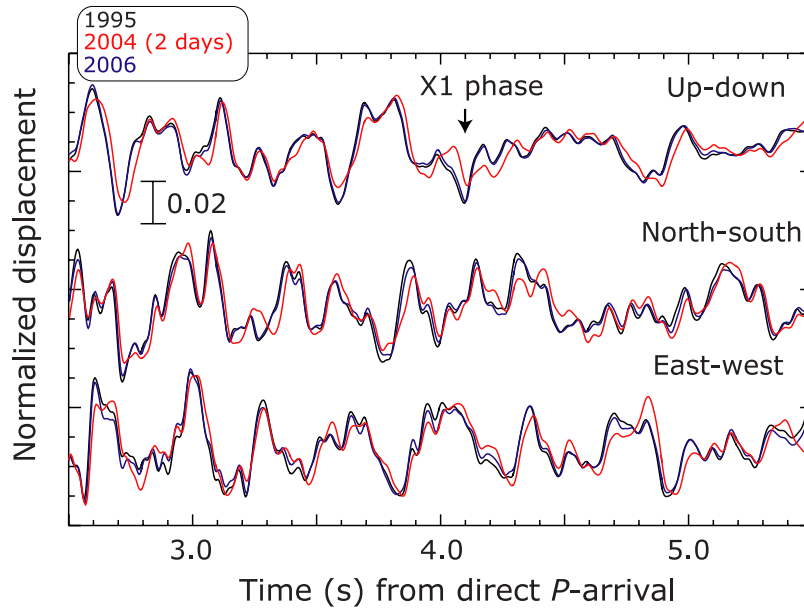


Figure 6. An example of observed three-component seismograms recorded at station VCA for the SE target sequence. Also shown in parentheses is elapsed day after the 2004 Parkfield earthquake.

but make the assumption that the shape of $P(\tau_i)$ remains the same. Such a distribution can be written as $P(a\tau_i)$, where a is a scale factor that is a function of the elapsed time after the 2004 Parkfield earthquake.

[27] If the mean and standard deviation of $P(\tau_i)$, are $\langle\tau_i\rangle$ and s_τ respectively, then we can always write $s_\tau = b|\langle\tau_i\rangle|$ for scale factor b . An important property of such a distribution is that b is independent of the time-dependent scale factor a . Thus the same proportionality holds for $P(a\tau_i)$, for any a . Since $\tau = \langle\tau_i\rangle$ and $D^{1/2} = \omega s_\tau / \sqrt{2}$, we obtain $\tau \propto D^{1/2}$. As such, we can rewrite the relationship between velocity and travelt ime in terms of $D(t)$ rather than $\tau(t)$, $|\langle\delta\nu\rangle|/V \propto D(t)^{1/2}/T$. Given that $\delta\nu/V$ is linearly related to $\sigma(t)$ at low stress levels [e.g., Sarkar et al., 2003], then we expect $D(t)^{1/2}$ to obey $D(t)^{1/2} \propto \sigma(t)$.

[28] The temporal behavior of $D(t)^{1/2}$ for time-varying scattered phases recorded at stations VCA and RMN are similar to each other, which is consistent with a change in medium. By combining $D(t)^{1/2}$ for stations VCA and RMN, we find that they correspond to a power law decay, $1/t^p$ with $p = 0.25 \pm 0.05$ (Figure 7), assuming all three time-varying scattered phases have the same time dependence, $\sigma(t)$.

2.3. Locations of Time-Dependent Scatterers

[29] We are particularly interested in determining whether temporal changes are shallow and most likely related to superficial damage/healing [Rubinstein and Beroza, 2005], or deeper and more closely related to seismogenic stress changes. To determine the location of the time-dependent scatterers, we established a source array consisting of one event from each the SAFOD target and repeated-aftershock sequences. We chose events well after the 2004 Parkfield earthquake so that we could incorporate the repeated-aftershock sequences. We assumed that the observed time variations in the scattered wavefield are caused by changes in properties of existing structures (i.e., opening or closing of existing fractures), although we cannot rule out the

possibility of new scatterers forming as a result of the 2004 Parkfield earthquake.

[30] We relocated the earthquakes in all six sequences by using a 3-D double difference relocation algorithm [Michelini and Lomax, 2003] with 3-D P and S wave velocity models for Parkfield [Michelini and McEvilly,

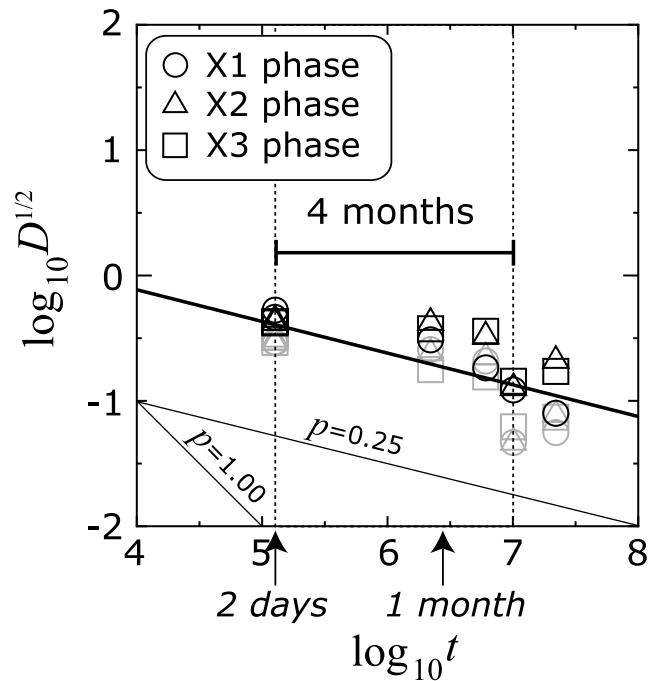


Figure 7. Square root of decorrelation indexes, $D(t)^{1/2}$, for X1 (circles), X2 (triangles), and X3 (squares) phases, as a function of the elapsed time (s) after the 2004 Parkfield earthquake. The data sets for stations VCA and RMN are shown by black and gray, respectively. Solid line indicates best fitting temporal decay trend.

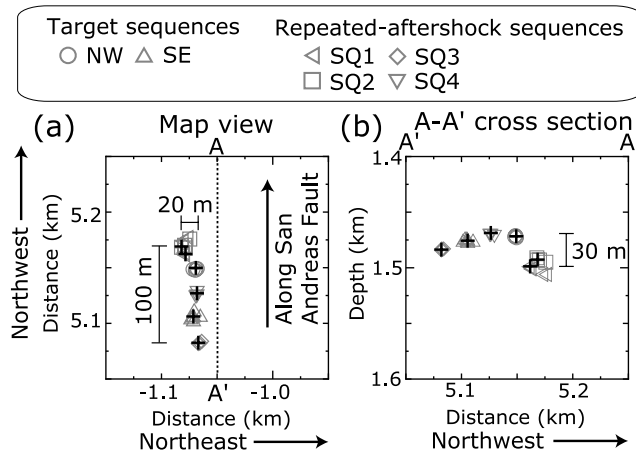


Figure 8. Geometry of the source array used in this study. (a) Map view of earthquakes and (b) the northwest-southeast cross section. The chosen earthquake in each sequence is shown as a cross. The coordinate center is the epicenter of the 1966 Parkfield earthquake.

1991]. The primary P and S wave velocity features of the velocity models we used are almost same as those of recent 3-D seismic velocity models [e.g., Roecker *et al.*, 2004; Thurber *et al.*, 2006]. The average uncertainty in relative earthquake location is less than 5 m in horizontal and vertical. The source array is located approximately 5 km northwest of the epicenter of the 1966 M 6 Parkfield earthquake and at a depth about 1.5 km (Figure 2). The source array extends about 100 m along strike, about 20 m across strike, and extends over a depth range of 30 m (Figure 8). This spatial extent among the earthquakes provides a means of spatially resolving the scatterers.

[31] The source array is a nearly vertical plane (Figure 8), and thus the array may have the poor azimuthal resolution. For example, apparent seismic velocities of two phases propagating horizontally along 30 and 330 degrees with respect to the strike of the plane could be similar to each other. On the other hand, the takeoff angle resolution of the source array should be better than its azimuthal resolution due to the vertical aperture size (30 m), and thus we should be able to distinguish between upgoing and downgoing waves.

[32] We used a scatterer-imaging methodology, similar to that of T. Taira *et al.* (Seismic imaging of scatterers at seismogenic depth, the San Andreas Fault, Parkfield, CA, manuscript in preparation, 2007), which can be used to estimate the scattering point through finding the maximum of the joint probability density function along with its 95% confidence region. As we noted above, the waveform similarities among the events are good enough for locating the time-dependent scatterers (Figure 9).

[33] The scattering mode of the X1, X2, and X3 phases was assumed to be S - P (Figure 6). We therefore used the vertical seismograms to locate the three scatterers. We additionally assumed a single scattering model to locate the scatterer position. We feel this assumption is justified for two reasons. First, excluding volcanic areas, the crust is normally assumed to be a weak scattering medium in which case multiple scattering effects can probably be neglected [Sato and Fehler, 1998]. Second, we focus on the temporal

behavior of discrete times in the coda. While multiple scatterers might play an important role in modulating the slow variation of $D(t)$ and $\tau(t)$ with elapsed time on the seismogram, we regard it as less likely to affect the temporal behavior of the X1, X2, and X3 phases that are the subject of this study.

[34] Using a semblance analysis [Neidell and Taner, 1971], we first calculated semblance values, $\Sigma(\theta, \varphi)$ in each scattered phase where θ and φ are the takeoff angle from vertical down and the azimuth clockwise from northwest. We evaluated the 95% confidence level of θ and φ based on the F distribution, which is similar to that of Silver and Chan [1991] for shear wave splitting. Following T. Taira *et al.* (manuscript in preparation, 2007), the confidence level of θ and φ can be expressed by

$$\frac{1 - \Sigma(\theta, \varphi)}{1 - \Sigma_{\max}} \leq 1 + \frac{k}{\nu - k} f_{k, \nu - k}(1 - \alpha), \quad (1)$$

where k and ν are the number of parameters and the degrees of freedom, respectively. Σ_{\max} is the maximum semblance value; f is the inverse of the F distribution, and $\alpha = 0.05$ corresponds to 95% confidence level. In our analysis, $k = 2$. On the other hand, ν can be formed in $\nu = 2f_w T_w$, where f_w is the band width of a band-pass filter and T_w is the length of a time window for calculating $\Sigma(\theta, \varphi)$ (T. Taira *et al.*, manuscript in preparation, 2007). Approximating the F distribution by a one-sided Gaussian probability density function (PDF), we obtained the probability density values, $P_{\Sigma}(\theta, \varphi)$:

$$P_{\Sigma}(\theta, \varphi) = \frac{2}{\sqrt{2\pi}s_{\Sigma}} \exp\left(-\frac{m^2}{2s_{\Sigma}^2}\right), \quad (2)$$

where

$$m = \frac{\nu - k}{k} \left\{ \left(\frac{1 - \Sigma(\theta, \varphi)}{1 - \Sigma_{\max}} \right) - 1 \right\}, \quad (3)$$

and s_{Σ} is the standard deviation of semblance values which can be written as $s_{\Sigma} = f_{k, \nu - k}(1 - \alpha)/2$ (T. Taira *et al.*, manuscript in preparation, 2007).

[35] We next estimated traveltimes residuals of the scattered phases between the observed, t^{obs} and predicted, t^{pre} traveltimes of a candidate scatterer originating from location, \mathbf{x} , based on the pseudobending method [Um and Thurber, 1987] with both 3-D P and S velocity structures [Michellini and McEvelly, 1991]. Assuming that the error in estimation of the traveltimes residual is a Gaussian PDF with the standard deviation, s_t , we obtained the probability density value for the traveltimes residual, $P_t(\mathbf{x})$:

$$P_t(\mathbf{x}) = \frac{1}{\sqrt{2\pi}s_t} \exp\left(-\frac{(t^{obs} - t^{pre})^2}{2s_t^2}\right). \quad (4)$$

[36] The 95% confidence region for the traveltimes residual can be defined by using $2s_t$; s_t is set to 0.25 s for our application.

[37] We finally calculated the joint probability density value, $P_f(\mathbf{x})$ by combining $P_{\Sigma}(\theta, \varphi)$ of equation (2) and $P_t(\mathbf{x})$ of equation (4). Here $P_{\Sigma}(\theta, \varphi)$ was converted into $P_{\Sigma}(\mathbf{x})$ in space by shooting the raypath with the slowness vector

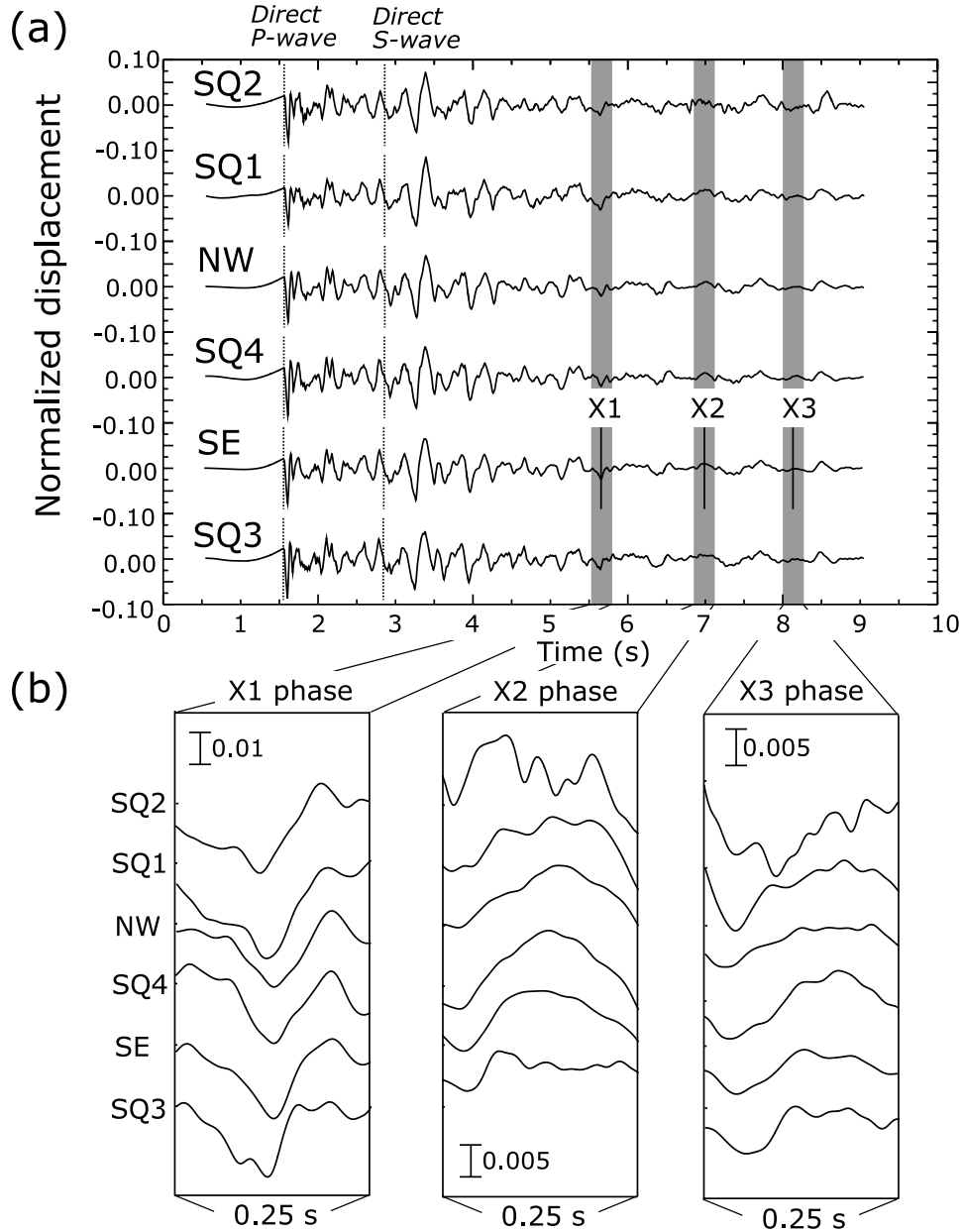


Figure 9. (a) An example of the vertical component array seismogram for station VCA and (b) enlarged views of X1, X2, and X3 phases. The traces are aligned with origin time from relocations and are ordered by hypocentral distances from station VCA (closest at the bottom).

$\kappa(\theta, \varphi)$. The wave type of the source-to-scatterer was assumed to be S for S - P scattering mode. The raypaths were determined based on the pseudobending method with the 3-D seismic velocity models. Using $P_{\Sigma}(\mathbf{x})$ and $P_l(\mathbf{x})$, $P_j(\mathbf{x})$ can be expressed by

$$P_j(\mathbf{x}) = P_{\Sigma}(\mathbf{x}) \cdot P_l(\mathbf{x}). \quad (5)$$

[38] Before applying the scatterer-imaging methodology, we reduced the errors in earthquake origin time by aligning the direct P arrival, t_p^{obs} , with respect to its predicted arrival time, t_p^{pre} , based on the calculated slowness by using the geometries of the source array and stations [e.g., Spudich and Bostwick, 1987], and then obtained the origin time

correction value, t_o defined as $t_p^{obs} - t_p^{pre}$. As a check of this origin time correction procedure, we measured the differential origin time correction value, δt_o between stations VCA and RMN for each earthquake; δt_o should be zero for an earthquake because the error in origin time should be station-independent. We, however, found that δt_o had a constant offset among the earthquakes, with an average value of -32.1 ms with standard deviation is 3.6 ms (Figure 10). We thus interpret δt_o as a path correction which can then be removed, and we regard the remaining 3.6 ms variation as the effective noise level in the traveltime measurements.

[39] The model space for scatterer location extends 20 km \times 20 km in the horizontal and 20 km in vertical.

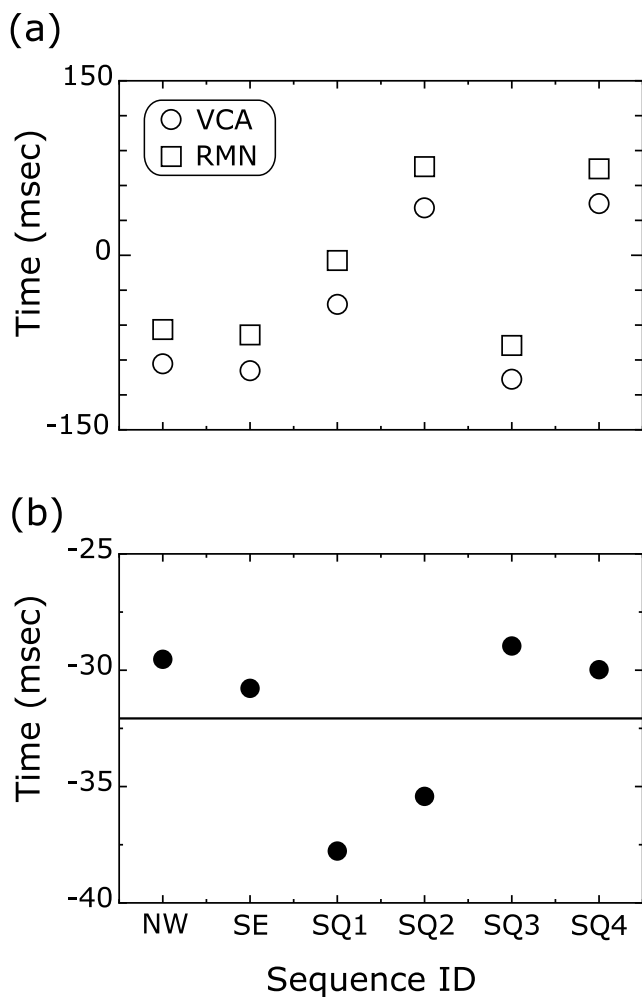


Figure 10. (a) Origin time correction values for stations VCA (circles) and RMN (squares) and (b) difference in the origin time correction values, δt_o , between these two stations. Solid line indicates the average of δt_o .

The coordinate center is the epicenter of the 1966 Parkfield earthquake and the coordinate system is rotated counterclockwise by 45 degrees (Figure 2). By analyzing the vertical component seismograms recorded at station VCA, we first estimated the locations of scatterers for X1, X2, and X3 phases, by utilizing the two probability densities for their slowness vectors and traveltimes, and then computed the predicted traveltimes of the three phases for station RMN. On the basis of these predicted traveltimes, we next chose the corresponding time-varying scattered phases for station RMN and estimated their joint probability densities.

[40] The source-to-scatterer slowness vector of each scattered phase should be independent of station. We found that estimated slowness vectors for station VCA are indeed compatible with those for station RMN (Figure 11). We finally determined each scatterer location by combining the two joint probability densities for stations VCA and RMN. The maxima of scattering points for X1, X2, and X3 phases are located close to the San Andreas Fault, and their depths are 11 km, 13 km, and 17 km, respectively, with uncertainty of ± 2 km (two standard deviations). These scattering points

are close to each other in the horizontal but at different depths (Figure 12).

[41] As mentioned above, we assumed *S-P* scattering mode for X1, X2, and X3 phases, based on our observation that all phases arrive in the *S* coda with dominant energy on the vertical component (Figure 6). We, however, examined the possibility that the X2 or X3 phase is caused by a different scattering mode from the same scatterer that produced X1 phase. By calculating the predicted traveltimes for *P-S* and *S-S* from this scatterer, we concluded that neither X2 nor X3 phase is consistent with this possibility.

3. Discussion

3.1. A Physical Mechanism for Time-Dependent Scatterers

[42] As shown in Figure 12, the estimated locations of the time-dependent scatterers are deeper than 10 km. This result suggests that the detected temporal changes in the scattered wavefield are not likely due to strong motion-induced cracks in subsurface layer, but rather due to much deeper modifications of the medium likely due to changes in the stress field.

[43] *Li et al.* [2006] examined that temporal changes in traveltimes (i.e., $\tau(t)$) from repeating earthquakes as well as repeated aftershocks following the 2004 Parkfield earthquake, showing that large traveltime changes were localized on the fault zone not only in the subsurface but also deeper as well (around 10 km depth). They showed that $\tau(t)$ exhibits a linear trend with elapsed time which is similar to our observation, interpreted as due to the opening of cracks caused by coseismic damage attributed with dynamic rupture of the 2004 Parkfield earthquake. Such cracks are small compared to a seismic wavelength.

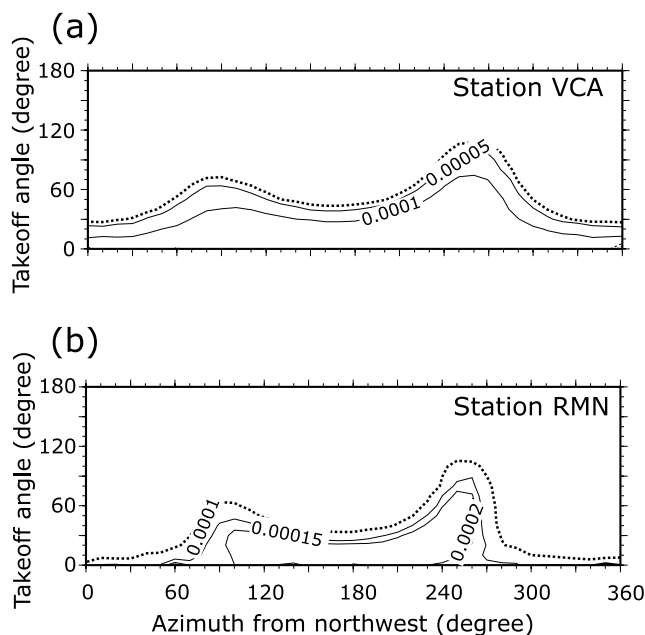


Figure 11. The 95% confidence regions of probability density for semblance values, $P_{\Sigma}(\theta, \phi)$, for phase X1 observed at stations (a) VCA and (b) RMN, as a function of takeoff angle θ and azimuth ϕ . Bold dashed contours correspond to the 95% confidence intervals.

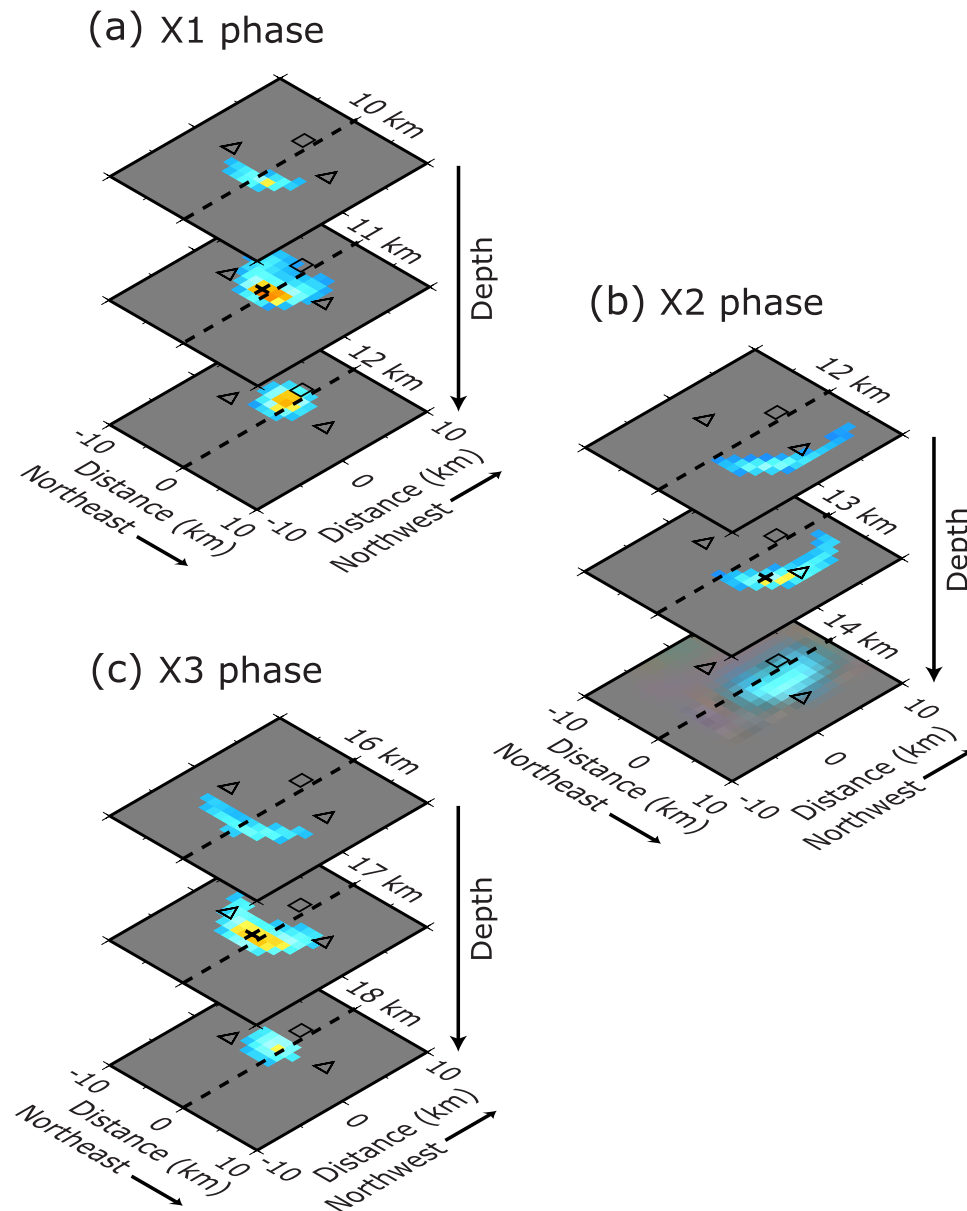


Figure 12. Depth slices of confidence regions of scattering points for (a) X1, (b) X2, and (c) X3 phases. The 95% confidence regions are shown by boundaries of colored regions. Warm colors indicate high-probability density values. Crosses are estimated locations. Square and triangles are the locations of the source array and the stations, respectively. Dashed lines are the projected surface trace of the San Andreas Fault.

[44] On the other hand, we found temporal changes in the waveform itself corresponding to isolated spikes in the decorrelation index and lag time (Figures 4 and 5). Such an isolated spike can be caused by a change in the location of a scatterer or by a velocity reduction near the scatterer [Niu *et al.*, 2003]. Under the interpretation of a single scatterer, the temporal change in the waveform we observe suggests changes in fractures that are comparable in size to a wavelength. Given the 5 Hz dominant frequency of the scattered phases (Figure 9), the detected time-dependent scatterers are likely fractures a few hundred meters in size, corresponding in size to the fault plane of a $M = 4$ earthquake. For another characteristic of the scatterers, namely the dominant S - P scattering mode, suggests that

the scatterers are fluid-filled fractures rather than dry ones [O'Connell and Budiansky, 1974]. Deep fractures tend to be closed by confining pressure, although fluid-filled fractures have been observed up to nearly 10 km [e.g., Huenges *et al.*, 1997].

[45] We compared the determined locations of time-dependent scatterers with coseismic (Figure 13a) and post-seismic slip distributions (Figure 13b) inverted from GPS and InSAR data [Johanson *et al.*, 2006] and the aftershock distribution [Thurber *et al.*, 2006] of the 2004 Parkfield earthquake. We also calculated Coulomb stress changes based on the coseismic slip model of Johanson *et al.* [2006], using Coulomb 2.5 [Toda and Stein, 2002]. Note that the coseismic slip includes 1-d of postseismic slip, and 40

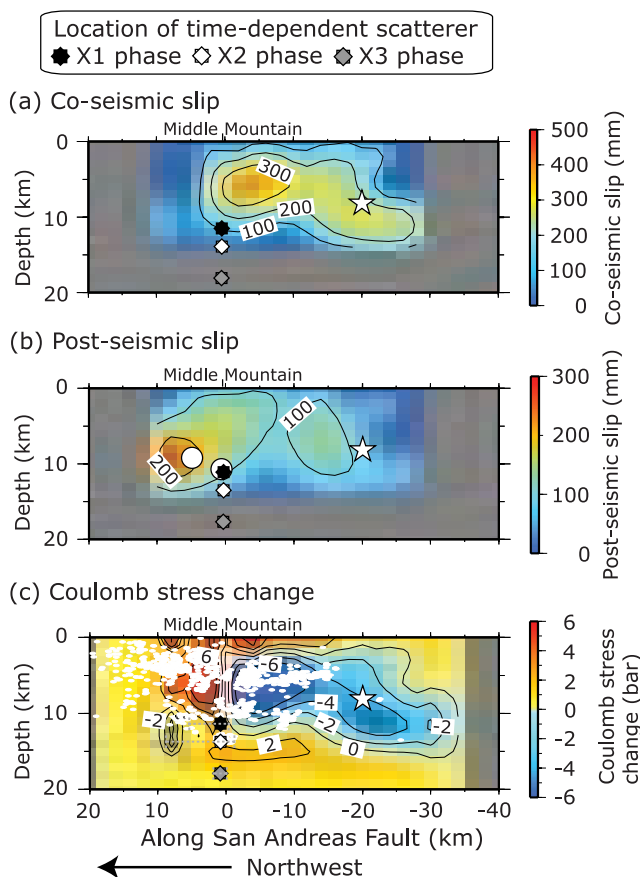


Figure 13. (a) Smoothed coseismic as well as (b) postseismic slip models of *Johanson et al.* [2006] and (c) calculated Coulomb stress changes based on the coseismic slip model with the locations of three time-dependent scatterers. Two standard deviation errors along the strike of the San Andreas Fault in those locations are shown by gray dashed bars in Figure 13c. Star is the hypocenter of the 2004 Parkfield earthquake. White circles in Figure 13b are the locations of two $M = 5$ aftershocks. White dots in Figure 13c are hypocenters of relocated aftershocks [Thurber et al., 2006] from 29 September 2004 through 30 June 2005.

to 55% of the coseismic slip could be aseismic [Johanson et al., 2006].

[46] The most prominent time-dependent scatterer for the X1 phase is likely located at the edge of significant coseismic slip (Figure 13a), where a stress concentration is predicted based on a Coulomb stress calculation (Figure 13c), and close to both the maximum in postseismic slip and the hypocenter of the $M = 5$ aftershock occurring on 29 September 2004 (Figure 13b). We suggest that this time-dependent scatterer is perturbed by a stress concentration due to coseismic slip which then decays back to the original state through the stress relaxation by postseismic slip, both seismic (aftershocks) and aseismic.

[47] The locations of the other two time-dependent scatterers corresponding to X2 and X3 phases are also in areas of predicted increased Coulomb stress (Figure 13c), which implies that they are also produced by a stress concentration following the 2004 Parkfield earthquake.

The time-dependent scatterer for X2 phase is likely located close to the deepest seismicity at 14 km depth in this region (Figure 13c). In this area, microearthquakes have been observed not only after the 2004 Parkfield earthquake but also in the interseismic period between the 1966 and 2004 Parkfield earthquake [e.g., Waldhauser et al., 2004; Bakun et al., 2005; Thurber et al., 2006]. This aftershock activity should reflect both a static stress concentration due to the coseismic slip as well as help to produce the subsequent stress relaxation near this time-dependent scatterer. Combining the aftershock activity and increased Coulomb stress, we conclude that the time dependence of X2 phase is a response to a coseismic stress perturbation and subsequent stress relaxation.

[48] For the time-dependent scatterer associated with the X3 phase, the depth (17 km) seems to be deeper than a transition depth between the locked zone and the creeping zone. *Rolandone et al.* [2004], however, showed that there are temporal changes in the transition depth between the locked and creeping zone following the 1992 $M 7.3$ Landers earthquake based on temporal changes in depth distribution of aftershocks. They found that the aftershock seismicity extended approximately 2 km deeper than seismicity before the Landers earthquake, and suggested that the deepening transition depth is caused by high postseismic stresses and strain rates following the 1992 Landers earthquake.

[49] Following *Rolandone et al.* [2004], we examined the temporal change in the depth distribution of seismicity. We estimated two parameters: the depth above which 95% of the earthquakes occur, $h_{95\%}$ and the average of the deepest 5% of earthquakes, $h_{5\%}$. We calculated $h_{95\%}$ and $h_{5\%}$ for a window including 1000 earthquakes, with a window overlap of 90%. We found a deepening aftershock distribution following the 2004 Parkfield earthquake (Figure 14), by using the relocated aftershock distribution [Thurber et al., 2006]. The depth of the seismic-aseismic transition changes by approximately 2 km, immediately after the 2004 Parkfield earthquake. Combining the deepening aftershock distribution and calculated Coulomb stress, we suggest that the physical mechanism of the time-dependent scatterers for X3 phase is similar to that for X1 and X2 phases.

[50] Seismic velocity reduction due to strong motion and coseismic slip of a main shock should cause an apparent deepening aftershock distribution. Such a reduction in S wave velocity was estimated to be around 1.5% within the fault zone at Parkfield and 0.5% outside the fault zone [Li et al., 2006]. Using the 1.5% value for the entire Parkfield area, an event located beneath Middle Mountain at 10 km depth can be shifted approximately 0.4 km deeper than its true location based on S - P time at station VCA, assuming a Poisson solid, while such apparent deepening of this event would be around 0.1 km for a 0.5% reduction. Since many seismic stations located far from the fault zone were used to relocate the aftershocks [Thurber et al., 2006], we expect that the apparent deepening of event location caused by seismic velocity reduction is around 0.1 km. We therefore conclude that the deepening of postearthquake seismicity is real.

3.2. Fault Zone Rheology

[51] Using the decorrelation index, $D(t)$, to represent the dissimilarity in waveforms, the temporal variation in $D(t)$

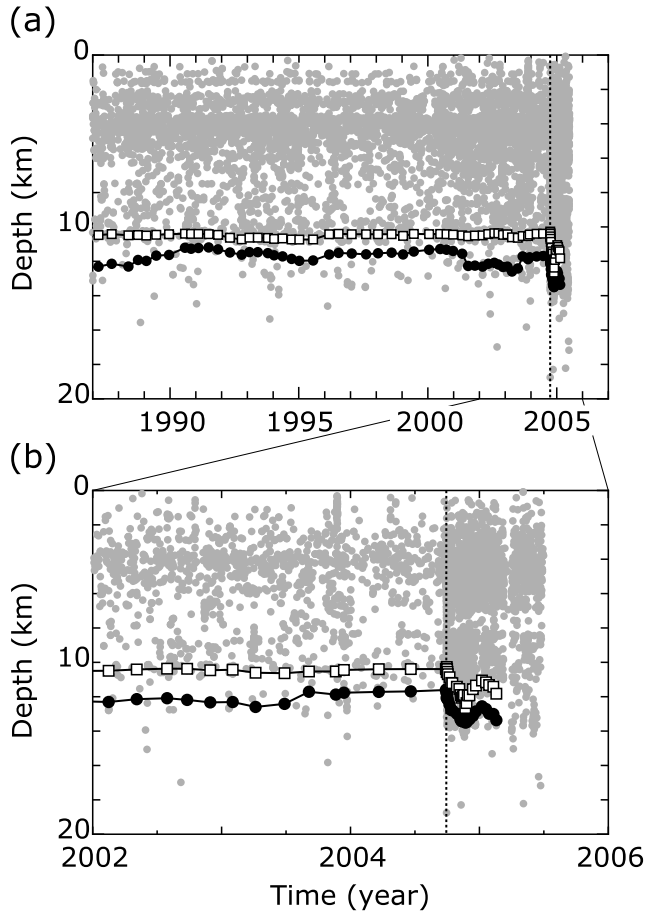


Figure 14. Temporal change in depth distribution of seismicity for the Parkfield segment (a) from 1987 through 2007 and (b) from 2002 through 2006. Solid circles and open squares show $h_{5\%}$ and $h_{95\%}$, respectively. Gray circles show earthquakes. The dashed line is the occurrence time of the 2004 Parkfield earthquake.

was examined by assuming a power law decay of the form, $1/t^p$. We used isolated spikes in $D(t)^{1/2}$ because we expect it to be proportional to stress. We found that its temporal behavior follows a power law with $p = 0.25 \pm 0.05$. Using a cross-correlation method, *Baisch and Bokelmann* [2001] examined the temporal decay rate of $D(t)$ from repeating earthquakes following the 1989 M 7.1 Loma Prieta earthquake. They showed that the temporal behavior is well explained by a power law decay with $p = 0.2$, corresponding to $p = 0.1$ for $D(t)^{1/2}$. Although the physical model and the location, particularly the depth of the temporal change was not well constrained, they suggested that the temporal change is related to opened cracks caused by the coseismic slip of the 1989 Loma Prieta earthquake.

[52] We also examined the temporal characteristics of the linear trend in lag time, $\tau(t)$, corresponding to seismic velocity changes in the background medium (Figure 4c). We calculated the linear trend in $\tau(t)$ in the S coda in order to avoid the effect of the clipped signals. The vertical component seismograms recorded at station VCA were used to measure the temporal behavior of $\tau(t)$ and the length of time window was 4.0 s from around 1.0 s after the direct S arrival. Assuming a power law decay, the value of exponent

p is 0.48 ± 0.09 . The difference in temporal behavior (i.e., p) between isolated spikes in $D(t)^{1/2}$ and linear trends in $\tau(t)$ may be a result of different physical mechanisms. The observed isolated spikes in $D(t)^{1/2}$ following the 2004 Parkfield earthquake should reflect on the stress relaxation process, as we discussed above (section 3.1), while a linear trend in $\tau(t)$ may be more strongly affected by damage and subsequent healing in surficial layers [e.g., *Rubinstein and Beroza*, 2005; *Li et al.*, 2006].

[53] As we showed earlier (section 2.2), we expect $D(t)^{1/2} \propto \sigma(t)$ and thus are able to evaluate the time evolution of the stress field in the fault zone at seismogenic depth. We can, in principle, constrain the fault zone rheology by comparing the time evolution of $\sigma(t)$ and strain rate, $\dot{\epsilon}(t)$, based on a power law rheology between $\sigma(t)$ and $\dot{\epsilon}(t)$ characterized by exponent n , i.e., $\dot{\epsilon}(t) = AH\sigma^n(t)$, where A is a preexponential factor depending on temperature and chemical environment while H is a shear zone thickness [e.g., *Evans and Kohlstedt*, 1995; *Montési*, 2004]. For dislocation creep, n ranges from 2 through 4 [e.g., *Kirby and Kronenberg*, 1987; *Hirth and Kohlstedt*, 2003], for diffusion creep, $n = 1$, and for frictional sliding, $n \gg 1$ [*Montési*, 2004]. *Freed and Bürgmann* [2004] examined the spatiotemporal evolutions of surface deformation following the 1992 M 7.3 Landers and the 1999 M 7.1 Hector Mine earthquakes, showing that a power law rheology model for the mantle with $n = 3.5$ matches well the observed GPS measurements.

[54] We took strain rate, $\dot{\epsilon}(t)$, to be proportional to GPS velocity, $V_{\text{GPS}}(t)$. To evaluate $\dot{\epsilon}(t)$, we used the 1-d solution for the two horizontal GPS velocities of *Langbein et al.* [2006], and made use of stations POMM and PKDB which are close to the locations of the time-dependent scatterers (Figure 2). Although GPS velocities can reveal time evolution of deformation with high-temporal resolution, they are most sensitive to shallow deformation. We therefore additionally examined slip rate, $\dot{d}(t)$, inferred from the recurrence intervals of repeating earthquakes [*Nadeau and McEvilly*, 1999, 2004], as a proxy for strain rate at greater depth.

[55] We made use of a cluster of repeating earthquakes at 5 km depth whose location is near that of the time-dependent scatterers (Figure 2). We found that the temporal behaviors of strain rates measured at the surface (i.e., $V_{\text{GPS}}(t)$) and at depth (i.e., $\dot{d}(t)$) are similar to each other (Figure 15). Assuming a power law decay, the exponent of p values for $\dot{d}(t)$ is $p = 0.8$, while these values for $V_{\text{GPS}}(t)$ range from 0.8 to 1.0. Given this similarity, we thus assumed that the time evolution of strain rate deeper than 10 km, where time-dependent scatterers are located, is similar to that reflected in $V_{\text{GPS}}(t)$. Estimated p values for $\dot{\epsilon}(t)$ is approximately 3–4 times larger than one for $D(t)^{1/2}$.

[56] Combining $D(t)^{1/2} \propto \sigma(t)$ and $V_{\text{GPS}}(t) \propto \dot{\epsilon}(t)$ into $\dot{\epsilon}(t) = AH\sigma^n(t)$, we obtain $V_{\text{GPS}}(t) = \gamma AHD(t)^{n/2}$ for constant γ , and then can determine stress exponent, n , by taking logarithm,

$$\log V_{\text{GPS}}(t) = \log C + \frac{n}{2} \log D(t),$$

where C is the product of A , H , and γ . We determined the best fitting n (and C) using a simultaneous inversion approach with the assumption that all three phases for stations VCA and RMN have the same value of n , but with

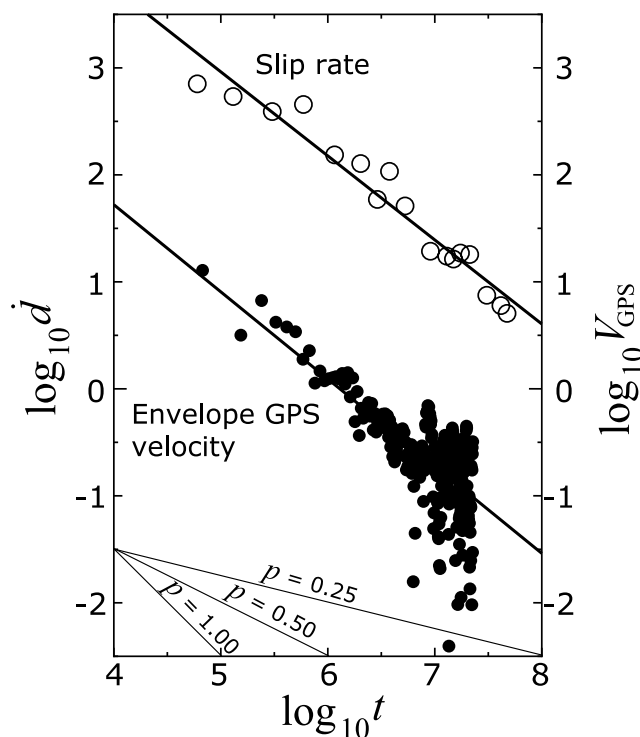


Figure 15. Slip rates at 5 km depth inferred from the recurrence intervals of repeating earthquakes (open circles) and GPS velocities from east-west component of station POMM (solid circles), as a function of the elapsed time (s) after the 2004 Parkfield earthquake. The solid lines indicate best fitting temporal decay trends. Each estimated slip rate was normalized by the value obtained for the interval September 1988 to October 1990, which was used as a reference. Envelope GPS velocities were computed by Hilbert transform.

different constant, C . We additionally estimated the confidence interval using a bootstrap technique [Efron and Tibshirani, 1993] where a subsampled data set is randomly sampled with replacement from the original data set. This process was repeated 1,000 subsamples and we estimated the 95% confidence interval for n , based on the standard deviation of these 1000 subsamples. We used $V_{\text{GPS}}(t)$ of two horizontal components at stations POMM and PKDB and $D(t)^{1/2}$ of the three time-varying phases (X1, X2, and X3) for the estimation of n .

[57] The estimated value of n is 2.5 (Figure 16) and its 95% confidence interval is 1.6–3.3. Our result for n implies that the fault zone rheology at the bottom of the seismogenic zone in the Parkfield segment can be characterized by ductile creep, rather than frictional sliding, for which a larger value of n would be expected [Montési, 2004]. The three phases and two stations also allow us to make 6 independent estimates of the stress exponent n . We found that these estimates range from 1.7 to 3.1. These values are consistent with each other within the uncertainties and thus do not exhibit detectable depth dependence. In addition, this similarity also suggests that our assumption that $D(t)^{1/2}$ is proportional to stress, is valid.

[58] We finally discuss the observable range of n for our data set. We defined the noise level of $D(t)^{1/2}$ as the

minimum observed value of $D(t)^{1/2}$ for the entire time period that we have analyzed. These minimum values are 0.08 and 0.05 for stations VCA and RMN, respectively. After an elapsed time of 26 d following the 2004 Parkfield earthquake, when a repeating earthquake in the SE sequence was detected, the observed values of $D(t)^{1/2}$ for stations VCA and RMN are about a factor of 5 higher than their noise levels (Figure 16). We can thus clearly distinguish between $n = 2.5$ and a lower value of n expected by the noise levels.

[59] The minimum value of n we could detect is probably $n \sim 1$. At this same period of time (26 d), the predicted $D(t)^{1/2}$ for $n = 1$ is about 0.05, which is comparable to the noise levels. We, however, expect that our estimation in the noise level is conservative because the estimated noise levels could still include real signal. Thus the signal-to-noise level is likely higher than our estimation, and therefore we would expect that $n \sim 1$ is probably detectable with our data set. On the other hand, detection of $n \gg 1$ should be easy, since it corresponds to the slow decay of $D(t)^{1/2}$. We conclude that our data set is indeed capable of detecting n ranging from $n \sim 1$ to $n \gg 1$.

4. Conclusions

[60] We have observed temporal changes in the scattered wavefield that was closely associated with the 2004 Parkfield earthquake, by using repeating earthquakes in SAFOD target sequences. These temporal changes were seen until 4 months after the 2004 Parkfield earthquake. After that, the observed waveforms are nearly identical to those before the 2004 Parkfield earthquake. We interpret these time-dependent scatterers as fluid-filled fractures

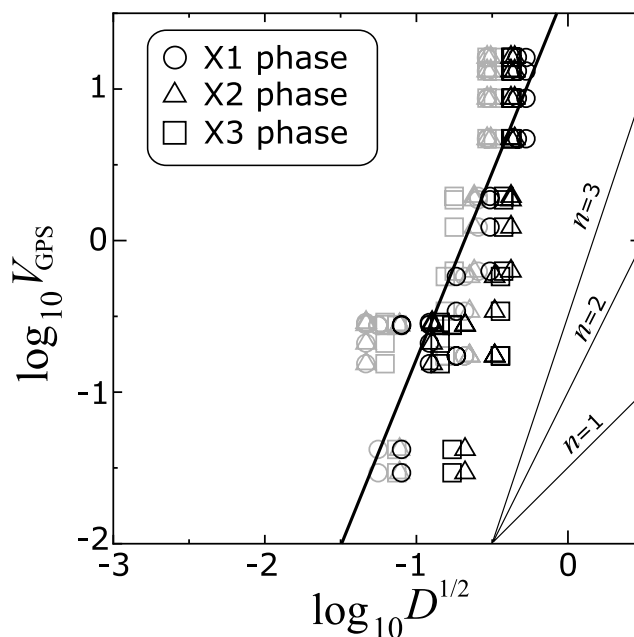


Figure 16. Comparison of time evolution of square root of decorrelation index, $D(t)^{1/2}$ with surface strain rate inferred from GPS velocities, $V_{\text{GPS}}(t)$. The data sets for stations VCA and RMN are shown by black and gray, respectively. Solid line is best fitting model.

whose size is a few hundred meters, based on the dominant S - P scattering mode and characteristic frequency of 5 Hz.

[61] We located time-dependent scatterers based on a source array analysis. The locations of time-dependent scatterers were well constrained, especially their depths, by combining slowness vectors and traveltimes of the scattered phases. The scatterers are likely located in the fault zone and close to Middle Mountain with depths greater than 10 km. They are thus likely related to changes in the seismogenic properties of the fault, rather than to shallow damage produced by coseismic shaking.

[62] As a possible physical mechanism of the time-dependent scatterers, we suggest that they are caused by localized stress changes due to the coseismic slip of the 2004 Parkfield earthquake, based on the calculated Coulomb stress change. In other words, we conclude that the changes are stress-induced. The most dominant time-dependent scatterer, X1, is located close to significant coseismic slip, as well as the maximum postseismic slip, and the location of a large $M = 5$ aftershock. This suggests that this time-dependent scatterer is produced by a stress concentration that was created by the coseismic slip and then subsequently decayed through both seismic and aseismic stress relaxation.

[63] We propose that the square root of the decorrelation index, $D(t)^{1/2}$, following the 2004 Parkfield earthquake, is linearly related to stress at depth, and can thus be used to constrain fault zone rheology, by combining stress with a strain rate estimated from GPS velocity. Assuming a power law rheology model, $\dot{\epsilon}(t) \propto \sigma^n(t)$, we estimated the stress exponent, n ranging from 1.6 through 3.3, which suggests that the rheology at the base of the seismogenic fault zone in the Parkfield segment of the San Andreas Fault can be characterized by dislocation creep.

[64] **Acknowledgments.** The Parkfield High-Resolution Seismic Network functions through close cooperation among researchers at the University of California, Berkeley, the U.S. Geological Survey (USGS), and the Lawrence Berkeley National Laboratory. The USGS currently provides primary financial support for the network through National Earthquake Hazards Reduction Program award 07HQAG0014. We would like to thank I. A. Johanson for providing us with the coseismic and postseismic slip models, and D. Mainprize and R. Bürgmann for discussions. The comments from the two anonymous reviewers improved the manuscript significantly. A software package, Generic Mapping Tools (GMT) [Wessel and Smith, 1995], was used to plot the figures. The present study was supported by the National Science Foundation EAR-0408947, EAR-0453638, EAR-0337308, and DTM-2025-01 and by the Department of Terrestrial Magnetism, Carnegie Institution of Washington.

References

- Baisch, S., and G. H. R. Bokelmann (2001), Seismic waveform attributes before and after the Loma Prieta earthquake: Scattering change near the earthquake and temporal recovery, *J. Geophys. Res.*, *106*(B8), 16,323–16,338.
- Bakun, W. H., et al. (2005), Implications for prediction and hazard assessment from the 2004 Parkfield, California, earthquake, *Nature*, *437*, 969–974, doi:10.1038/nature04067.
- Dodge, D. A., and G. C. Beroza (1997), Source array analysis of coda waves near the 1989 Loma Prieta, California, mainshock: Implications for the mechanism of coseismic velocity changes, *J. Geophys. Res.*, *102*, 24,437–24,458.
- Efron, B., and R. J. Tibshirani (1993), *An Introduction to the Bootstrap*, *Monogr. Stat. Appl. Probab.*, vol. 57, Chapman and Hall, New York.
- Eshelby, J. (1957), The determination of the elastic field of an ellipsoidal inclusion, and related problems, *Proc. R. Soc. London, Ser. A*, *241*, 376–396.
- Evans, B., and D. L. Kohlstedt (1995), Rheology of rocks, in *Rock Physics and Phase Relations: A Handbook of Physical Constants, Ref. Shelf*, vol. 3, edited by T. J. Ahrens, pp. 148–165, AGU, Washington, D. C.
- Freed, A. M., and R. Bürgmann (2004), Evidence of power-law flow in the Mojave desert mangle, *Nature*, *430*, 548–551, doi:10.1038/nature02784.
- Freund, D. (1992), Ultrasonic compressional and shear velocity in dry elastic rocks as a function of porosity, clay content and confining pressure, *Geophys. J. Int.*, *108*, 125–135.
- Grêt, A., R. Snieder, and J. Scales (2006), Time-lapse monitoring of rock properties with coda wave interferometry, *J. Geophys. Res.*, *111*, B03305, doi:10.1029/2004JB003354.
- Hirth, G., and D. L. Kohlstedt (2003), Rheology of the upper mantle and the mantle wedge: A view from the experimentalists, in *The Subduction Factory*, *Geophys. Monogr. Ser.*, vol. 138, edited by J. Eiler, pp. 83–105, AGU, Washington, D. C.
- Huenges, E., J. Erzinger, J. Kück, B. Engeser, and W. Kessels (1997), The permeable crust: Geohydraulic properties down to 9101 m depth, *J. Geophys. Res.*, *102*, 18,225–18,265.
- Johanson, I. A., E. J. Fielding, F. Rolandone, and R. Bürgmann (2006), Coseismic and postseismic slip of the 2004 Parkfield earthquake from space-geodetic data, *Bull. Seismol. Soc. Am.*, *96*(4B), S269–S282, doi:10.1785/0120050818.
- Karageorgi, E., R. Clymer, and T. V. McEvelly (1992), Seismological studies at Parkfield: II. Search for temporal variations in wave propagation using Vibroseis, *Bull. Seismol. Soc. Am.*, *82*(3), 1388–1415.
- Kirby, S. H., and A. K. Kronenberg (1987), Rheology of the lithosphere: Selected topics, *Rev. Geophys.*, *25*, 1219–1244.
- Langbein, J., et al. (2005), Preliminary report on the 28 September 2004, M 6.0 Parkfield, California earthquake, *Seismol. Res. Lett.*, *76*(1), 10–26.
- Langbein, J., J. R. Murray, and H. A. Snyder (2006), Coseismic and initial postseismic deformation from the 2004 Parkfield, California, earthquake, observed by Global Positioning System, electronic distance meter, creepmeters, and borehole strainmeters, *Bull. Seismol. Soc. Am.*, *96*(4B), S304–S320, doi:10.1785/0120050823.
- Li, Y.-G., J. E. Vidale, K. Aki, F. Xu, and T. Burdette (1998), Evidence of shallow fault zone strengthening after the 1992 M 7.5 Landers, California, earthquake, *Science*, *279*, 217–219, doi:10.1126/science.279.5348.217.
- Li, Y.-G., P. Chen, E. S. Cochran, J. E. Vidale, and T. Burdette (2006), Seismic evidence for rock damage and healing on the San Andreas Fault associated with the 2004 M 6.0 Parkfield earthquake, *Bull. Seismol. Soc. Am.*, *96*(4B), S349–S363, doi:10.1785/0120050803.
- Liu, P., S. Custódio, and R. J. Archuleta (2006), Kinematic inversion of the 2004 M 6.0 Parkfield earthquake including an approximation to site effects, *Bull. Seismol. Soc. Am.*, *96*(4B), S143–S158, doi:10.1785/0120050826.
- Michelini, A., and A. Lomax (2003), Velocity structure effects in double-difference earthquake location, *Geophys. Res. Abstr.*, *5*, Abstract 09550.
- Michelini, A., and T. V. McEvelly (1991), Seismological studies at Parkfield: I. Simultaneous inversion for velocity structure and hypocenters using B-splines parameterization, *Bull. Seismol. Soc. Am.*, *81*(2), 524–552.
- Montési, L. G. J. (2004), Controls of shear zone rheology and tectonic loading on postseismic creep, *J. Geophys. Res.*, *109*, B10404, doi:10.1029/2003JB002925.
- Nadeau, R. M., and T. V. McEvelly (1999), Fault slip rates at depth from recurrence intervals of repeating microearthquake, *Science*, *285*, 718–721, doi:10.1126/science.285.5428.718.
- Nadeau, R. M., and T. V. McEvelly (2004), Periodic pulsing of characteristic microearthquakes on the San Andreas Fault, *Science*, *303*, 200–202, doi:10.1126/science.1090353.
- Nadeau, R. M., A. Michelini, R. A. Uhrhammer, D. Dolenc, and T. V. McEvelly (2004), Detailed kinematics, structure and recurrence of microseismicity in the SAFOD target region, *Geophys. Res. Lett.*, *31*, L12S08, doi:10.1029/2003GL019409.
- Neidell, N. S., and M. T. Taner (1971), Semblance and other coherency measures for multichannel data, *Geophysics*, *36*, 482–497.
- Niu, F., P. G. Silver, R. M. Nadeau, and T. V. McEvelly (2003), Migration of seismic scatterers associated with the 1993 Parkfield aseismic transient event, *Nature*, *426*, 544–548, doi:10.1038/nature02151.
- O'Connell, R. J., and B. Budiansky (1974), Seismic velocities in dry and saturated cracked solids, *J. Geophys. Res.*, *79*, 5412–5426.
- Peng, Z., and Y. Ben-Zion (2006), Temporal changes of shallow seismic velocity around the Karadere-Düzce branch of the north Anatolian fault and strong ground motion, *Pure Appl. Geophys.*, *163*, 567–599, doi:10.1007/s00024-005-0034-6.
- Roecker, S., C. Thurber, and D. McPhee (2004), Joint inversion of gravity and arrival time data from Parkfield: New constraints on structure and hypocenter locations near the SAFOD drill site, *Geophys. Res. Lett.*, *31*, L12S04, doi:10.1029/2003GL019396.
- Rolandone, F., R. Bürgmann, and R. M. Nadeau (2004), The evolution of the seismic-aseismic transition during the earthquake cycle: Constraints from the time-dependent depth distribution of aftershocks, *Geophys. Res. Lett.*, *31*, L23610, doi:10.1029/2004GL021379.

- Rubinstein, J. L., and G. C. Beroza (2004), Evidence for widespread nonlinear strong ground motion in the M_w 6.9 Loma Prieta earthquake, *Bull. Seismol. Soc. Am.*, *94*(5), 1595–1608, doi:10.1785/012004009.
- Rubinstein, J. L., and G. C. Beroza (2005), Depth constraints on nonlinear strong ground motion from the 2004 Parkfield earthquake, *Geophys. Res. Lett.*, *32*, L14313, doi:10.1029/2005GL023189.
- Sarkar, D., A. Bakulin, and R. L. Kranz (2003), Anisotropic inversion of seismic data for stressed media: Theory and a physical modeling study on Berea Sandstone, *Geophysics*, *68*, 690–704, doi:10.1190/1.1567240.
- Sato, H., and M. C. Fehler (1998), *Seismic Wave Propagation and Scattering in the Heterogeneous Earth*, Springer, New York.
- Silver, P. G., and W. W. Chan (1991), Shear wave splitting and subcontinental mantle deformation, *J. Geophys. Res.*, *96*, 16,429–16,454.
- Silver, P. G., T. M. Daley, F. Niu, and E. L. Majer (2007), Active source monitoring of crosswell seismic travel time for stress-induced changes, *Bull. Seismol. Soc. Am.*, *97*(1B), 281–293, doi:10.1785/0120060120.
- Snieder, R., A. Grêt, H. Douma, and J. Scales (2002), Coda wave interferometry for estimating nonlinear behavior in seismic velocity, *Science*, *295*, 2253–2255, doi:10.1126/science.1070015.
- Spudich, P., and T. Bostwick (1987), Studies of the seismic coda using an earthquake cluster as a buried seismograph array, *J. Geophys. Res.*, *92*, 10,526–10,546.
- Toda, S., and R. S. Stein (2002), Response of the San Andreas fault to the 1983 Coalinga-Nuñez earthquake: An application of interaction-based probabilities for Parkfield, *J. Geophys. Res.*, *107*(B6), 2126, doi:10.1029/2001JB000172.
- Thurber, C., H. Zhang, F. Waldhauser, J. Hardebeck, and A. Michaels (2006), Three-dimensional compressional wavespeed model, earthquake relocations, and focal mechanisms for the Parkfield, California, region, *Bull. Seismol. Soc. Am.*, *96*(4B), S38–S49, doi:10.1785/0120050825.
- Um, J., and C. Thurber (1987), A fast algorithm for two-point seismic ray tracing, *Bull. Seismol. Soc. Am.*, *77*(3), 972–986.
- Vidale, J. E., and Y.-G. Li (2003), Damage to the shallow Landers fault from the nearby Hector Mine earthquake, *Nature*, *421*, 524–526, doi:10.1038/nature01354.
- Waldhauser, F., W. L. Ellsworth, D. P. Schaff, and A. Cole (2004), Streaks, multiplets, and holes: High-resolution spatio-temporal behavior of Parkfield seismicity, *Geophys. Res. Lett.*, *31*, L18608, doi:10.1029/2004GL020649.
- Wessel, P., and W. H. F. Smith (1995), New version of the Generic Mapping Tool released, *Eos Trans. AGU*, *76*(33), 329.
- Yamamura, K., O. Sano, H. Utada, Y. Tekei, S. Nakao, and Y. Fukao (2003), Long-term observation of in situ seismic velocity and attenuation, *J. Geophys. Res.*, *108*(B6), 2317, doi:10.1029/2002JB002005.

R. M. Nadeau, Berkeley Seismological Laboratory, University of California, Berkeley, 215 McCone Hall, Berkeley, CA 94720, USA. (nadeau@seismo.berkeley.edu)

F. Niu, Department of Earth Science, Rice University, 6100 Main Street, Houston, TX 77005, USA. (niu@rice.edu)

P. G. Silver and T. Taira, Department of Terrestrial Magnetism, Carnegie Institution of Washington, 5241 Broad Branch Road, N.W., Washington, DC 20015, USA. (silver@dtm.ciw.edu; taira@dtm.ciw.edu)